T. Guillet, C. Zucchetti, A. Marchionni, A. Hallal, P. Biagioni, C. Vergnaud, A. Marty, H. Okuno, A. Masseboeuf, M. Finazzi, F. Ciccacci, M. Chshiev, F. Bottegoni, and M. Jamet, *Spin orbitronics at a topological insulator-semiconductor interface.* PHYSICAL REVIEW B **101**,184406 (2020).

Spin-orbitronics at a topological insulator-semiconductor interface

T. Guillet,[1, *] C. Zucchetti,[2, *] A. Marchionni,[2] A. Hallal,[1] P. Biagioni,[2] C. Vergnaud,[1] A. Marty,[1]
H. Okuno,[3] A. Masseboeuf,[1] M. Finazzi,[2] F. Ciccacci,[2] M. Chshiev,[1] F. Bottegoni,[2] and M. Jamet[1]

[1]*Univ. Grenoble Alpes, CEA, CNRS, Grenoble INP, IRIG-Spintec, 38000 Grenoble, France*
[2]*LNESS-Dipartimento di Fisica, Politecnico di Milano,*
Piazza Leonardo da Vinci 32, 20133 Milano, Italy
[3]*Univ. Grenoble Alpes, CEA, IRIG-MEM, 38000 Grenoble, France*
(Dated: March 27, 2020)

Topological insulators (TIs) hold great promises for new spin-related phenomena and applications thanks to the spin texture of their surface states. However, a versatile platform allowing for the exploitation of these assets is still lacking due to the difficult integration of these materials with the mainstream Si-based technology. Here, we exploit germanium as a substrate for the growth of Bi_2Se_3, a prototypical TI. We probe the spin properties of the Bi_2Se_3/Ge pristine interface by investigating the spin-to-charge conversion taking place in the interface states by means of a non-local detection method. The spin population is generated by optical orientation in Ge, and diffuses towards the Bi_2Se_3 which acts as a spin detector. We compare the spin-to-charge conversion in Bi_2Se_3/Ge with the one taking place in Pt in the same experimental conditions. Notably, the sign of the spin-to-charge conversion given by the TI detector is reversed compared to the Pt one, while the efficiency is comparable. By exploiting first-principles calculations, we ascribe the sign reversal to the hybridization of the topological surface states of Bi_2Se_3 with the Ge bands. These results pave the way for the implementation of highly efficient spin detection in TI-based architectures compatible with semiconductor-based platforms.

I. INTRODUCTION

In the past decade, the discovery of topological insulators (TIs) has promised a breakthrough in the efficiency of spin-charge interconversion phenomena. Indeed, TIs are known to host topologically-protected surface states (TSS) leading to spin-momentum locking [1]. This has been experimentally verified by means of photoemission measurements [2, 3], scanning tunneling microscopy, and magnetotransport experiments [4–6]. In particular, spin-momentum locking in TSS leads to the conversion of a charge current into a spin current, a phenomenon that is commonly addressed as the Rashba-Edelstein effect (REE), while the reverse process is referred to as the inverse Rashba-Edelstein effect (IREE) [7]. In these systems, the leading parameters are the spin-charge interconversion efficiencies: $q_{REE} = j_s^{3D}/j_c^{2D}$ for the REE and $\lambda_{IREE} = j_c^{2D}/j_s^{3D}$ for the IREE. However, an experimental estimation based on spin pumping-ferromagnetic resonance (FMR) or spin torque-FMR [8–10] is questionable, since TIs are known to chemically react when they are in contact with a ferromagnetic film [11, 12]. Therefore, a non-local architecture where the source of the spin current and the TI are well separated would represent a reliable route to avoid the aforementioned issue.

In this work, we use germanium as a platform for such non-local spin-to-charge conversion (SCC) measurements. The spin population is generated by optical spin orientation in Ge, and diffuses as a spin current towards the Bi_2Se_3, which acts as the spin detector. In this way,

we totally avoid any ferromagnetic material to generate the spin current. We probe SCC at the Bi_2Se_3/Ge interface kept at room temperature and compare the experimental results with those obtained from a Pt/Ge junction in the same experimental conditions. The measurements at the Pt/Ge junction allow us to test and validate our microscopic models of spin injection, transport and non-local detection using Ge(111) as a platform. Indeed platinum is a prototypical material for spin-to-charge conversion by the inverse spin Hall effect (ISHE) with well-known spin Hall angle. We first estimate the SCC efficiency at the Bi_2Se_3/Ge interface, which is found to be of the same order of magnitude as the one of Pt. We then develop microscopic models for spin injection, transport and non-local detection to evaluate the conversion efficiency of the IREE in the junction and find $\lambda_{IREE} \approx -30$ pm. Notably, the sign of the SCC is opposite to the one of Pt. To understand this sign reversal, we employ first principles calculations and demonstrate the existence of Rashba states at the Bi_2Se_3/Ge interface as a result of strong interfacial hyridization. We find that these states exhibit an opposite spin chirality compared to the one of TSS in bulk-terminated Bi_2Se_3.

II. DESCRIPTION OF THE SAMPLES AND METHODS

As a substrate, we use a 2 μm-thick n-doped Ge(111) layer (doping concentration $N_d = 9 \times 10^{16}$ cm^{-3}) epitaxially grown on semi-insulating Si.

The 10-nm thick Bi_2Se_3 film is grown on the Ge(111) layer by molecular beam epitaxy in the van der Waals regime [13]. (111)-oriented germanium exhibits the
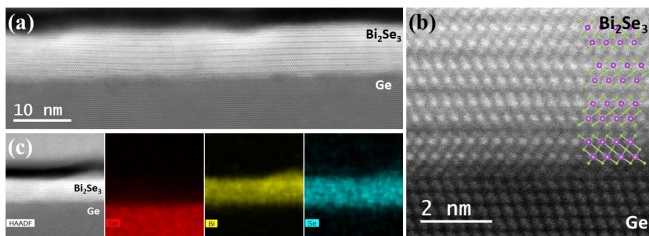
FIG. 1. (Color online) (a) Low and (b) High magnification transmission electron microscopy cross-section images of the Bi_2Se_3/Ge interface showing the atomic sharpness and epitaxial relationship. (c) Energy-dispersive x-ray spectroscopy of the Bi_2Se_3/Ge stack. From the high-angle annular dark-field (HAADF) image, we extracted the elemental maps of Ge, Bi and Se.

proper six-fold symmetry and lattice constant to grow epitaxially high quality crystalline Bi_2Se_3 thin films. During the growth, the surface quality and structure is followed by reflection high-energy electron diffraction (RHEED). Before the growth of Bi_2Se_3, the Ge(111) surface was annealed up to $850°C$ under ultrahigh vacuum (UHV) ($p \approx 5 \times 10^{10}$ mbar) in order to remove the native germanium oxide. Then, we used soft argon etching and performed a subsequent annealing to obtain the Ge(2×8) surface reconstruction. We first deposit one monolayer of Bi at room temperature and annealed the substrate until the $Bi/Ge(111)$-($\sqrt{3} \times \sqrt{3})R30°$ surface reconstruction appeared in the RHEED pattern. This Bi layer prevents the reaction of Ge with Se. Bi_2Se_3 is then grown by co-depositing Bi and Se at a substrate temperature of $220°C$. Bi and Se are evaporated using an e-beam evaporator and a Knudsen cell, respectively. Bi and Se evaporation rates are adjusted in order to reach a high Se:Bi ratio of about 15:1 and limit the presence of Se vacancies in the film. At the end of the growth, a 2 nm-thick aluminum layer is grown on top to prevent the Bi_2Se_3 from oxidation in air. As illustrated in Fig. 1(a) and 1(b) by cross-sectional transmission electron microscopy, we obtain a very sharp Bi_2Se_3/Ge interface with the $Bi_2Se_3(110)||Ge(1\bar{1}0)$ epitaxial relationship. The energy dispersive x-ray spectroscopy maps shown in Fig. 1(c) confirm the elemental sharpness of the interface with only little selenium diffusion in the first atomic planes of germanium. The 15 nm-thick Pt spin detector is also grown in UHV by e-beam evaporation following the same procedure to prepare a clean Ge(111) surface prior to the Pt deposition. The RHEED pattern exhibits rings showing the polycrystalline character of the Pt film. After the growth, we process the samples into small devices shown in Fig. 2(a) to perform non-local spin-to-charge conversion measurements. To do so, we first spin-coat a photosensitive resist on the samples and use laser lithography (at λ=380 nm) to define the 75×10 μm^2 Bi_2Se_3 and Pt detection bars using ion beam etching and soft O_2 plasma cleaning. After a re-alignment pro-

cedure, a 15 nm-thick Pt layer is deposited by e-beam evaporation using the lift-off technique to define the 20×2 μm^2 stripes which are exploited for optical spin injection [14, 15]. The distance between the stripes is 10 μm. In a third step, a 70 nm-thick insulating SiO_2 layer is deposited by ion beam sputtering and lift-off between Ge and the Au/Ti contacts to insulate them from the Ge substrate and prevent direct spin absorption by the contacts. Finally, the Au(120 nm)/Ti(5 nm) pads are deposited by e-beam evaporation and lift-off to contact the Bi_2Se_3 or Pt central detection bar. In this procedure, the interface between the Pt stripes for optical spin orientation and Ge is ill defined due to the lift-off process with the probable presence of Ge oxide. It makes those stripes bad spin sinks as compared to the central Bi_2Se_3 and Pt detection bars. We can thus consider the spin absorption by those stripes to be very small.

The measurements have been performed at room temperature using a confocal microscope, shown in Fig. 2(b). The circularly polarized laser spot is scanning the sample to generate locally a spin accumulation in germanium. In the confocal microscope, the energy of the photons is tuned to the direct Ge gap ($\hbar\omega = 0.8$ eV) and the circular polarization of the light is modulated by a photoelastic modulator (PEM) at 50 kHz. The light is then focused on the sample by an objective with a 0.7 numerical aperture, yielding a laser spot of full-size diameter on the sample of about 3 μm. The voltage drop ΔV is then obtained by demodulating with a lock-in amplifier the signal acquired under open-circuit conditions between the Ti/Au (see Fig. 2(a)) while the focused light beam raster scans the sample surface.

The working principle of the non-local spin-injection/detection scheme is illustrated in Fig. 2(c).

The spin injection is based on the optical spin orientation in Ge [16]. It consists in the absorption of circularly-polarized light that generates spin-polarized electron-hole pairs at the Γ point of the Brillouin zone. The spin polarization of photogenerated electrons in the conduction band is $P = (n_\uparrow - n_\downarrow)/(n_\uparrow + n_\downarrow)$, being $n_{\uparrow(\downarrow)}$ the spin-up (-down) densities referred to the quantization axis given by the direction of the light wavevector in the material. Photogenerated holes are rapidly depolarized due to their very short spin lifetime [17]. If the incident photon energy is tuned to the direct Ge bandgap, an electron spin polarization $P = 50$ % can be achieved [18]. Right after the photogeneration, spin-oriented electrons thermalize from the Γ to the L valleys within approximately 300 fs, maintaining most of their spin polarization [19]. In the microscope, the laser beam impinges the sample at normal incidence and only an out-of-plane spin polarization is generated by optical spin orientation in Ge, preventing any electrical spin detection by the Bi_2Se_3 or Pt bars. The Pt stripes allow us to circumvent this limitation, as already demonstrated in Ref. [14]. In short, when the sample is illuminated with circularly polarized light focused at the edge of a Pt stripe, the x component E_x of the electric field induces charges that generate in
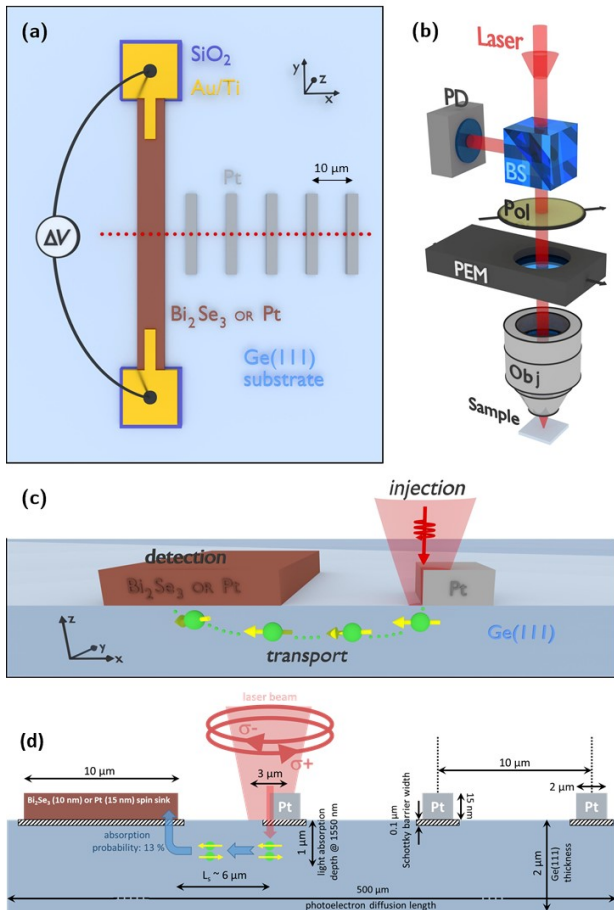
FIG. 2. (Color online) (a) Sample layout. The vertical brown bar represents the spin-detector and is made either of Bi_2Se_3 or platinum. The bar is electrically contacted by two Ti/Au pads. (b) Confocal microscopy setup. PD, BS, Pol and PEM represent the photodetector, beam splitter, polarizer and photo-elastic modulator respectively. (c) Spin generation and diffusion in Ge(111). (d) Schematics of the device in cross-section summarizing all the dimensions and relevant characteristic lengths.

the Ge substrate a near-field with a large component in the z direction. The latter is in antiphase with respect to E_x because the illumination wavelength of 1550 nm is significantly shorter than those corresponding to the main plasmonic resonances of the Pt stripe. The combination of the z component of the near-field with the $\pi/2$ phase-shifted y component E_y of the incoming light results in an elliptic field polarization in the yz plane that can generate electrons with spin polarization along the x axis. Opposite spin polarizations are attained at opposite edges of the Pt stripes. To estimate the fraction of photons with in-plane angular momentum when light impinges the edge of a platinum stripe, three-dimensional numerical simulations have been performed by applying finite-difference time-domain simulations [14, 20].

We reproduce the experimental illumination conditions, with complex dielectric constants $\epsilon_{Ge} = 19 + i\,0.087$ and $\epsilon_{Pt} = -21.36 + i\,74.8$ for Ge and Pt, respectively [21]. The Stokes parameter $c_x = 2\,\mathrm{Im}\{E_z E_y^*\}$ is calculated inside the Ge substrate when the focus of the light beam is centered on the edge of a Pt microstructure. In this geometry, the fraction of photons with a projection of the angular momentum along the x-axis of the sample is estimated as the ratio between the integral of c_x and the integral of the total electric field intensity $I = E_x^2 + E_y^2 + E_z^2$ over the volume of the Ge film. The result is further normalized to the fraction of impinging photons that are absorbed in Ge, yielding to a final value of $\eta_g = 2.2\,\%$. The resulting spin accumulations at Pt stripe edges create spin currents directed to the detection bar with in-plane polarization which are converted into a transverse voltage drop ΔV caused by the ISHE [22] in the case of detection with Pt, and by the IREE [7] in the case of Bi_2Se_3. In both cases, the geometry of spin-to-charge conversion imposes ΔV to be sensitive only to an electron spin polarization directed along the x-axis [15, 24]. In our analysis, we consider that the spin current is absorbed at the edge of the detector: we make the assumption of a point contact absorption [23]. We show in section III that only 13 % of the electron spins are absorbed because of the presence of the Schottky barrier even if it is reduced by the photovoltaic effect. The electron spins enter the detector by thermionic emission. The Schottky barrier being the same for the Bi_2Se_3 and Pt detectors due to the Fermi level pinning by Ge surface states, the fraction of spins entering the detectors (13 %) for diffusion and absorption is exactly the same for both materials without spin backflow. Concerning the effect of the detector size, in our setup, we detect a spin voltage at the modulating frequency of the photoelastic modulator in open circuit conditions. The conversion of the spin current into a transverse charge current into the Bi_2Se_3 or Pt detector generates a current which, multiplied by the resistance between the two probe contacts, gives the measured voltage. The resistance obviously depends on the width of the detector. For a detector width w, the resistance and thus the detected voltage will decrease linearly with w. Here, we have chosen a large detector width of 10 µm for technical reasons: using laser lithography, it is difficult to define top contacts (made of Au/Ti) on bars smaller than 10 µm. By the way, as shown in section III, the signals we detect are well above the noise level (some tens of µV), they are reproducible and lead to reasonable physical values. In Fig. 2(d), we summarize the device dimensions and give characteristic lengths of the system: the electron spin diffusion length ($L_s \approx 6.0$ µm, see section III), the photoelectron diffusion length at $\lambda=1550$ nm (500 µm [25]), the light absorption length at $\lambda=1550$ nm (1 µm [25]) and the Schottky barrier width (0.1 µm) corresponding to the n-type doping of the Ge film.

III. NON-LOCAL SPIN-TO-CHARGE CONVERSION MEASUREMENTS

We first show the results obtained on the sample with the Bi_2Se_3 detector. The reflectivity and the electrical maps are shown in Fig. 3(a) and (b), respectively [26]. The electrical map is normalized to the impinging laser power W. As expected for a spin-related signal, by illuminating at opposite edges the Pt stripes used for spin injection, the sign of the electric signal is reversed. This can be better visualized in Fig. 4 that shows the profiles, integrated along the y-axis, of the reflectivity [panel (a)] and electrical maps [panel (b)]. From the latter, we also observe the decrease of the absolute value of the signal when the generation point (i.e., the edge of the illuminated Pt stripe) moves away from the Bi_2Se_3 bar. This signal decay is related to the spin depolarization from the generation to the detection point, which is larger for longer paths [15]. This is illustrated in Fig. 4 (c) that reports $|\Delta V_{IREE}|$ measured at each Pt edge as a function of the distance x from the position of the Bi_2Se_3 detector. Even though the Pt stripes are not good spin sink as discussed in the previous section, we can nevertheless consider that they absorb a small amount of the spins accumulated beneath. In that case, we can still use a simple unidimensional spin-diffusion model with a single exponential function: $\Delta V_{IREE} \propto e^{-x/L_s}$ [15] to fit the experimental data as shown in Fig. 4 (c). However, the estimated spin diffusion length $L_s = 5.8 \pm 0.7$ µm corresponds to an effective value shorter than the actual spin diffusion length in bulk Ge as already discussed in Ref. [15]. This value is indeed slightly shorter than the one reported for Ge(001) substrates with similar doping [27].

The same analysis, summarized in Fig. 5, has been performed for the sample with the Pt detector. Panels (a,b) show the reflectivity and the normalized ISHE map of the sample, respectively, while in panels (c,d) we report the profiles along the x axis of the two maps. In panel (e), we plot $|\Delta V_{ISHE}|$ at each Pt edge as a function of the distance from the spin detector. We find $L_s = 6.0 \pm 1.1$ µm, which perfectly matches the value obtained with the Bi_2Se_3 sample. Following the same discussion as for Bi_2Se_3, this value can be considered as an effective spin diffusion length.

Since the spin-injection and transport mechanisms are the same for the two samples, it is possible to quantitatively compare the results obtained with Bi_2Se_3 and Pt detectors. First, from Fig. 4(a,b), we observe that the Bi_2Se_3 detection provides a negative (positive) voltage drop when the focused light beam illuminates the left (right) edge of the Pt injection stripes. Conversely, when SCC is performed via the ISHE in Pt, the signal is positive (negative) at the left (right) edge of the injector microstructures [see Fig. 5(c,d)]. Hence, the sign of the spin-to-charge conversion in Bi_2Se_3/Ge is found to be opposite to that in Pt. Previous experiments were performed to characterize the spin-to-charge conversion in Bi_2Se_3 thin films [8–10] and, at variance with our re-
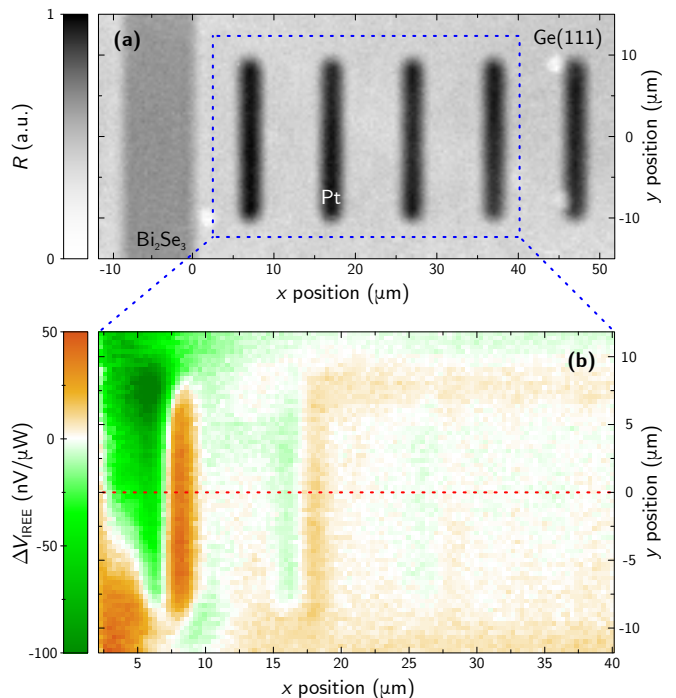

FIG. 3. (Color online) Reflectivity (a) and IREE map (b) of the Bi_2Se_3/Ge(111) junction acquired for an incident power $W = 18$ µW at $\hbar\omega = 0.8$ eV. The IREE map is collected over the area identified by the dashed blue rectangle in the upper panel.
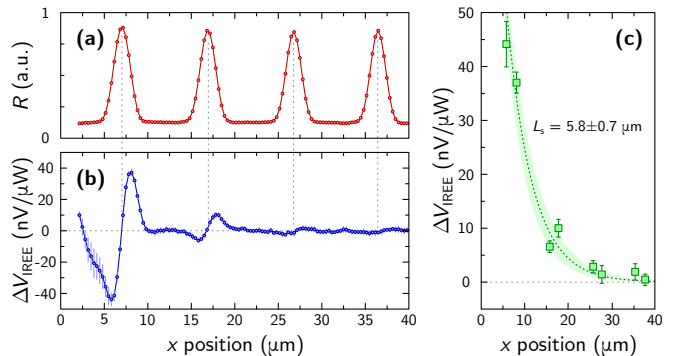

FIG. 4. (Color online) Reflectivity (a) and IREE (b) profiles signal along the x-axis of the sample. (c) $|\Delta V_{IREE}|$ as a function of x. ΔV_{IREE} is negative for the left edges of the Pt stripes whereas ΔV_{IREE} is positive for the right edges. The data are associated by pairs corresponding to each Pt stripe.

sult, the conversion parameter was always measured with the same sign as ISHE in Pt, which we arbitrarily define as "positive". Although the SCC measurements in Refs. 8–10 were carried out with the TI in direct contact with a ferromagnet, this positive sign is also expected from photoemission spectroscopy [2, 28] and electrical spin detection [29, 30]. Hence, as further discussed in the following, our experimental results suggest that the
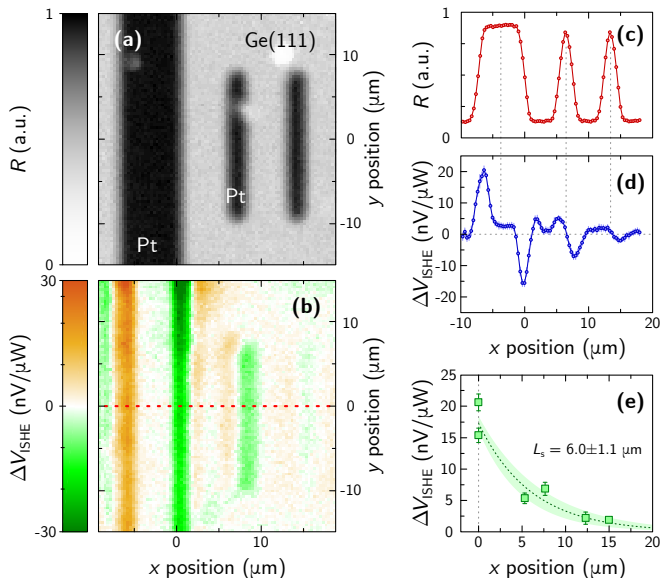
FIG. 5. (Color online) Reflectivity (a) and ISHE map (b) of the Pt/Ge(111) sample acquired for $W = 15$ μW at $\hbar\omega = 0.8$ eV. Reflectivity (c) and ISHE (d) profiles along the x-axis of the sample. (e) $|\Delta V_{\text{ISHE}}|$ as a function of x. ΔV_{ISHE} is positive for the left edges of the Pt stripes whereas ΔV_{ISHE} is negative for the right edges. The data are associated by pairs corresponding to each Pt stripe.

spin-split states at the Bi_2Se_3/Ge(111) interface display a substantially different SCC behavior compared to the ones of a freestanding Bi_2Se_3 surface.

Beyond this sign reversal, the comparison of Fig. 4(c) and Fig. 5(e) allows one to estimate the relative spin detection efficiency of Bi_2Se_3/Ge and Pt. With the light beam focused on the first Pt stripe ($x = x_0 \approx 6$ μm), we measure $\Delta V_{\text{IREE}}/W \approx 40$ nV/μW for Bi_2Se_3/Ge and $\Delta V_{\text{ISHE}}/W \approx 7$ nV/μW for Pt. Since the two samples only differ by the spin detector, we conclude that the overall efficiency for spin detection with Bi_2Se_3/Ge is a factor 5 larger than with Pt. The insulating character of bulk TIs indeed produces higher voltage drops compared to a metal like Pt for the same charge current.

The macroscopic spin-to-charge conversion parameter is $\gamma = i_c/i_s$, being i_s the spin current entering the detector and i_c the equivalent charge current across the detection bar, defined as the ratio between the open circuit ISHE or IREE signal ΔV and the detector resistance R, $i_c = \Delta V/R$. If we assume the same value of i_s for the two samples (due to equal spin injection and transport mechanisms), the relative spin-to-charge conversion efficiency of the materials is $\gamma_{\text{BiSe}}/\gamma_{\text{Pt}} = i_{c,\text{BiSe}}/i_{c,\text{Pt}}$. Considering the ΔV values recorded at $x = x_0 \approx 6$ μm and being $R_{\text{BiSe}} \approx 10$ kΩ and $R_{\text{Pt}} \approx 500$ Ω the detector resistance, as measured by a four-probe technique, we obtain $\gamma_{\text{Pt}} \approx -3.5 \gamma_{\text{BiSe}}$. Here, we stress the fact that R_{BiSe} and R_{Pt} account for the possible current shunting in the Ge channel. However, the electrical current i_c is only sourced

in the Bi_2Se_3 or Pt bar. The absolute determination of γ requires the knowledge of i_s. To estimate its value, we start from the spin current excited at the generation time:

$$i_{s,0} = \frac{TW}{\hbar\omega} P \eta_g,$$ (1)

where $TW/\hbar\omega$ is the photon absorption rate ($T \approx 0.6$ is the transmittance of Ge at $\hbar\omega = 0.8$ eV and W the impinging light power), $\eta_g = 2.2$ % (see section II) and $P = 50$ % [16] is the ratio between spin-polarized photo-generated electrons and absorbed photons. The spin current reaching the position of the detector is $i_{s,0}\, e^{-x_0/L_s}$, the exponential term accounting for the spin depolarization along the distance x_0 from the generation point to the detector.

Because of the built-in electric field in the Schottky barrier at the Bi_2Se_3/Ge and Pt/Ge junctions, only a fraction η_t of the spin-polarized electrons reaching the detector position effectively enters the detector and thus contributes to the measured signal. As shown in Fig. 2(d), the thickness of the depleted region is of the order of 0.1 μm at equilibrium without illumination. At this stage, we consider the Bi_2Se_3 and Pt detectors as identical spin sinks without spin backflow to Ge due to the high Schottky barrier. We calculate η_t by applying the same numerical simulations as the ones detailed in Ref. [31, 32]. They consist in solving self-consistently the coupled (spin resolved) drift-diffusion-Poisson equations with the Nextnano software [33]. The calculations take into account the electrostatic effects due to the Schottky barrier, the photovoltaic effect and the internal Dember field. In particular, the Schottky barrier reduction Φ_{ph} produced by the photovoltaic effect and extending over hundreds of μm (see Fig. 2(d)) is found to be 0.29 eV. In the simulations, we clearly see that the optically-induced spin density gradient between the semiconductor and the detector allows for the injection of spins across the Schottky barrier by means of thermionic emission. In the numerical model, we introduce the Schottky barrier height measured by magnetotransport measurements: $\Phi_{\text{bar}} \approx 0.66$ eV. We find the same value for both Bi_2Se_3/Ge and Pt/Ge junctions as expected from the Fermi level pinning for Ge surfaces [34]. With all these parameters, we finally obtain $\eta_{t,\text{BiSe}} = \eta_{t,\text{Pt}} = 13$ %. Since the spin injectors (Pt stripes), the substrate where spins diffuse, the height of the Schottky barrier and the geometrical characteristics are rigorously the same for both the $BiSe_3$/Ge and the Pt/Ge heterostructures, the electrical spin-to-charge conversion signal as well as the sign, coming from the two samples can be properly compared. We validate the numerical model with Pt, for which the spin Hall angle has been addressed by several works in the literature. In this case, we have measured $\Delta V_{\text{ISHE}}/W = 7$ nV/μW (obtained for an incident optical power $W = 15$ μW) at $x = x_0 \approx 6$ μm, corresponding to $i_c = \Delta V_{\text{ISHE}}/R = 210$ pA. Our numerical estimation of i_s yields $i_s = 6$ nA, giving $\gamma_{\text{Pt}} = i_c/i_s \approx 3.5$ %.

This value is comparable to previously reported ones for evaporated Pt films [35, 36], therefore we apply the same model to the sample with a Bi$_2$Se$_3$ detector. At $x = x_0 \approx 6$ μm, we obtain $\Delta V_{\text{IREE}}/W = -40$ nV/μW (measured with $W = 18$ μW). Hence $i_c = -72$ pA and $i_s = 7.2$ nA, yielding $\gamma_{\text{BiSe}} \approx -1\%$.

Since the spin-to-charge conversion by the IREE occurs in surface states, the relevant parameter describing the SCC efficiency is the inverse Rashba-Edelstein length λ_{IREE}, which can be obtained as the product between the macroscopic efficiency parameter γ_{BiSe} and the spatial extension d of the surface or interface states in which the conversion takes place. Taking this spatial extension to be $d = 3$ nm from Ref. 28, we find $\lambda_{\text{IREE}} = \gamma_{\text{BiSe}} d \approx -30$ pm. Note that, to derive λ_{IREE} from γ_{BiSe}, we only need to consider SCC occurring in the Bi$_2$Se$_3$ surface states in contact with Ge and neglect SCC at the opposite Bi$_2$Se$_3$ free surface, since the film is thicker than the spin diffusion length [37].

IV. FIRST PRINCIPLES CALCULATIONS

In order to understand the opposite SCC signs for the two samples, we have performed first principle relativistic calculations to unveil the spin-resolved band structure at the Bi$_2$Se$_3$/Ge interface [38]. We first consider eight quintuple layers (8 QL) of Bi$_2$Se$_3$. In Fig. 6(a), the band structure is plotted along the K-Γ-M direction as shown in the inset. In this particular direction along which K-Γ (Γ-M) is parallel to the x (y) direction, we plot the band structure weighted by the y (x) spin component S_y (S_x) of the topmost QL, as highlighted by the thick red and blue lines. The red (blue) color indicates an in-plane spin pointing in the positive (negative) direction of the axis. We clearly observe the presence of surface states belonging to Dirac cones. Due to spin-momentum locking characteristic of TIs, the in-plane spin helicity of the surface states above the Dirac point (characterized by a positive dispersion) displays a clockwise (CW) chirality, while the helicity of states below the Dirac point (with a negative dispersion) is counterclockwise (CCW). Because of the opposite dispersion relation, both types of chiral states (either above or below the Dirac point) thus lead to a *positive* λ_{IREE} value and to the same sign of the SCC coefficient as the one observed in platinum [39].

Figure 6(b) displays the band structure of 8 QL of Bi$_2$Se$_3$ in contact with 3.2 nm of Ge. Compared with pure Bi$_2$Se$_3$, many additional electronic states appear due to the strong hybridization with Ge. In Fig. 6(b), we use the same color code as in Fig. 6(a) to highlight the spin texture at the Bi$_2$Se$_3$/Ge interface. Interestingly, due to the strong hybridization between Bi$_2$Se$_3$ and Ge orbitals, the bottom Dirac cone is inverted. This cone inversion gives rise to a Rashba-like helical spin texture exhibiting a counter-clockwise (CCW) chirality of the outer contour for -0.05 eV $< E - E_{\text{DP}} <$ 0.15 eV, E_{DP} being the energy of the Dirac point. Therefore, in
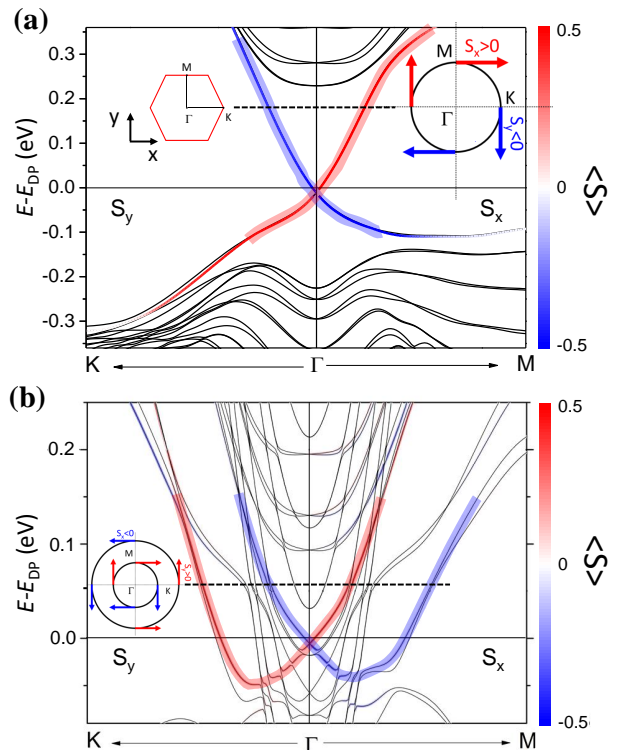

FIG. 6. (Color online) (a) Electronic band structure with spin-orbit coupling for 8 QL of Bi$_2$Se$_3$. The red and blue colors indicate the spin texture of the topmost QL projected along the y and x direction for the K-Γ and Γ-M high symmetry axes, respectively. The corresponding Brillouin zone as well as a specific spin-resolved Fermi contour are reported in the insets. (b) Electronic band structure for the Bi$_2$Se$_3$ (8 QL)/Ge (3.2 nm) stack. The same color code as in (a) is used for the interface spin texture. The inset shows a specific spin-resolved Fermi contour. E_{DP} corresponds to the energy position of the Dirac point of Bi$_2$Se$_3$ surface states in (a) and Bi$_2$Se$_3$/Ge interface states in (b).

this energy range, the CCW spin chirality of the outer contour leads to a *negative* λ_{IREE} value. First principles calculations thus qualitatively support our experimental observations concerning the sign of the spin-charge conversion. It should also be noticed that, by adjusting the position of the Fermi level in Fig. 6(b) with a gate voltage to the Bi$_2$Se$_3$/Ge heterostructure, it could be possible to control both the magnitude and the sign of the spin-to-charge conversion at the interface.

V. CONCLUSION

To summarize, we have probed the spin-to-charge conversion at the Bi$_2$Se$_3$/Ge interface by using a non-local spin injection/detection scheme. Notably, we measure

larger voltage drops with Bi_2Se_3 than with the Pt reference, which makes the former an excellent spin detector for future spin-based technologies. We have numerically modeled the spin injection and transport in Ge to the Bi_2Se_3 detector and found an equivalent spin-Hall angle close to the one derived for Pt. It corresponds to an inverse Rashba-Edelstein length $\lambda_{IREE} \approx -30$ pm. The sign of the spin-to-charge conversion is found to be opposite for Bi_2Se_3/Ge and Pt. By employing first principles calculations, we ascribe this behavior to the interfacial hybridization between the topologically protected surface states of Bi_2Se_3 and Ge leading to the formation of Rashba interface states with a spin chirality opposite to the one of states at the free Bi_2Se_3 surface. Our results demonstrate that semiconductors constitute a very promising platform for the exploitation of topological insulators in spintronics, where, by gating the heterostructure, spin-to-charge conversion could in principle be tuned in magnitude and sign.

[1] M. Z. Hasan and C. L. Kane, Rev. Mod. Phys. **82**, 3045 (2010).
[2] D. Hsieh *et al.*, Nature **460**, 1101 (2009).
[3] H. Zhang, C.-X. Liu, X.-L. Qi, X. Dai, Z. Fang, and S.-C. Zhang, Nat. Phys. **5**, 438 (2009).
[4] Y. S. Kim, M. Brahlek, N. Bansal, E. Edrey, G. A. Kapilevich, K. Iida, M. Tanimura, Y. Horibe, S.-W. Cheong, and S. Oh, Phys. Rev. B. **84**, 073109 (2011).
[5] M. Liu *et al.*, Phys. Rev. Lett. **108**, 036805 (2012).
[6] M. Lang *et al.*, Nano. Lett. **13**, 48 (2012).
[7] V. M. Edelstein *et al.*, Solid State Comm. **73**, 233 (1990).
[8] M. Jamali, J. S. Lee, J. S. Jeong, F. Mahfouzi, Y. Lv, Z. Zhao, B. K. Nikolic, K. A. Mkhoyan, N. Samarth, and J.-P. Wang, Nano. Lett. **15**, 7126 (2015).
[9] S. Shi *et al.*, Phys. Rev. B. **97**, 041115(R) (2018).
[10] H. Wang, J. Kally, J. S. Lee, T. Liu, H. Chang, D. R. Hickey, K. A. Mkhoyan, M. Wu, A. Richardella, and N. Samarth, Phys. Rev. Lett. **117**, 076601 (2016)
[11] L. A. Walsh, C. M. Smyth, A. T. Barton, Q. Wang, Z. Che, R. Yue, J. Kim, M. J. Kim, R. M. Wallace, and C. L. Hinkle, J. Phys. Chem. C **121**, 23551 (2017).
[12] K. Ferfolja, M. Valant, I. Mikulska, S. Gardonio, and M. Fanetti, J. Phys. Chem. C **122**, 9980 (2018).
[13] T. Guillet, A. Marty, C. Beigné, C. Vergnaud, M.-T. Dau, P. Noël, J. Frigerio, G. Isella, and M. Jamet, AIP Adv. **8**, 115125 (2018).
[14] F. Bottegoni, M. Celebrano, M. Bollani, P. Biagioni, G. Isella, F. Ciccacci, and M. Finazzi, Nat. Mat. **13**, 790 (2014).
[15] C. Zucchetti *et al.*, Phys. Rev. B. **96**, 014403 (2017).
[16] *Optical Orientation*, edited by F. Meier and B. P. Zakharchenya (North-Holland, Amsterdam, 1984.
[17] F. Rortais, S. Oyarzún, F. Bottegoni, J.-C. Rojas-Sánchez, P. Laczkowski, A. Ferrari, C. Vergnaud, C. Ducruet, C. Beigné, N. Reyren, A.Marty, J.-P. Attané, L. Vila, S. Gambarelli, J. Widiez, F. Ciccacci, H. Jaffrès, J.-M. George, and M. Jamet, J. Phys.: Condens. Matter **28**, 165801 (2016).
[18] J. Rioux and J. E. Sipe, Phys. Rev. B **81**, 155215 (2010).
[19] F. Pezzoli, F. Bottegoni, D. Trivedi, F. Ciccacci, A. Giorgioni, P. Li, S. Cecchi, E. Grilli, Y. Song, M. Guzzi, H. Dery, and G. Isella, Phys. Rev. Lett. **108**, 156603 (2012).
[20] FDTD Solutions 2018b, v. 8.20.1634, Lumerical Inc., Canada.
[21] E. D. Palik, Handbook of optical constants of solids, Academic Press (1998).
[22] M. I Dyakonov and V. I. Perel, Phys. Lett. A **35**, 459 (1971).
[23] P. Laczkowski *et al.*, Phys. Rev. B **92**, 214405 (2015).
[24] K. Ando, M. Morikawa, T. Trypiniotis, Y. Fujikawa, C. H. W. Barnes, and E. Saitoh, J. Appl. Phys. **107**, 113902 (2010).
[25] See: http://www.ioffe.ru/SVA/NSM/Semicond/Ge/
[26] The IREE map of Fig. 3(b) does not include the area straddling the Bi_2Se_3 detector, since the IREE signal obtained by illuminating the edges of the Bi_2Se_3 stripe cannot be directly compared with the one generated at Pt stripe edges, due to the different materials involved in the optical spin injection process. Nevertheless, the corresponding data are shown in the Supplementary Material [38].
[27] C. Zucchetti, M. Bollani, G. Isella, M. Zani, M. Finazzi, and F. Bottegoni, APL Mater. **7**, 101122 (2019).
[28] M. Neupane *et al.*, Nat. Comm. **5**, 3841 (2014).
[29] C. H. Li, O. M. J. van't Erve, J. T. Robinson, Y. Liu, L. Li, and B. T. Jonker, Nat. Nanotechnol. **9**, 218 (2014).
[30] J. S. Lee, A. Richardella, D. R. Hickey, K. A. Mkhoyan, and N. Samarth, Phys. Rev. B **92**, 155312 (2015).
[31] I. Zutic, J. Fabian, and S. Das Sarma, Phys. Rev. B **64**, 121201 (2001).
[32] G. Isella, F. Bottegoni, A.Ferrari, M. Finazzi, and F. Ciccacci, Appl. Phys. Lett. **106**, 232402 (2015).
[33] S. Birner, T. Zibold, T. Andlauer, T. Kubis, M. Sabathil, A. Trellakis, and P. Vogl, IEEE Trans. Electron Dev. **54**, 2137 (2007).
[34] A. Dimoulas, P. Tsipas, A. Sotiropoulos, and E. K. Evangelou, Appl. Phys. Lett. **89**, 252110 (2006).
[35] E. Sagasta, Y. Omori, M. Isasa, M. Gradhand, L. E. Hueso, Y. Niimi, Y. C. Otani, and F. Casanova, Phys. Rev. B **94**, 060412(R) (2016).
[36] Y. Huo, F. L. Zeng, C. Zhou, and Y. Z. Wu, AIP Adv. **7**, 056024 (2017).
[37] P. Deorani, J. Son, K. Banerjee, N. Koirala, M. Brahlek, S. Oh, and H. Yang, Phys. Rev. B **90**, 094403 (2014).
[38] Supplementary Material can be found at: http://
[39] J.-C. Rojas-Sánchez *et al.*, Phys. Rev. Lett. **116**, 096602 (2016).